



ATLAS NOTE

ATLAS-CONF-2015-020

26th June 2015



Measurement of two-particle pseudorapidity correlations in lead–lead collisions at $\sqrt{s_{\text{NN}}} = 2.76$ TeV with the ATLAS detector

The ATLAS Collaboration

Abstract

Two-particle pseudorapidity correlations are measured using charged particles from $\sqrt{s_{\text{NN}}} = 2.76$ TeV Pb+Pb collisions collected in 2010 by the ATLAS experiment at the LHC, corresponding to an integrated luminosity of $7 \mu\text{b}^{-1}$. The correlation function $C_N(\eta_1, \eta_2)$ is measured for different centrality intervals as a function of the pseudorapidity of the two particles, η_1 and η_2 , for $|\eta| < 2.4$ and transverse momentum $p_T > 0.5$ GeV. An enhancement is observed along $\eta_- \equiv \eta_1 - \eta_2 \approx 0$ and a suppression is observed at large η_- values. The correlation function also shows a characteristic quadratic dependence along the $\eta_+ \equiv \eta_1 + \eta_2$ direction. These structures are consistent with a strong forward-backward asymmetry of the particle multiplicity that fluctuates event to event. The correlation function is expanded in terms of products of Legendre polynomials $T_n(\eta_1)T_m(\eta_2)$, and corresponding coefficients $a_{n,m}$ are measured. These are related to mean-square values of the Legendre coefficients, a_n , at the single particle level: $a_{n,m} = \langle a_n a_m \rangle$. Significant values are observed for $\langle a_n^2 \rangle$ and mixed terms $\langle a_n a_{n+2} \rangle$, which decrease quickly for larger n . The leading coefficient a_1 is compared to that estimated from a fit to $C_N(\eta_+)$ for different η_- slices, as well as to the asymmetry of the number of participating nucleons between the two colliding nuclei.



1 Introduction

Heavy-ion collisions at RHIC and the LHC create hot, dense matter whose space-time evolution can be well described by relativistic viscous hydrodynamics. Due to the strong event-by-event (EbyE) density fluctuations in the initial state, the space-time evolution of the produced matter in the final state also fluctuates event to event. These fluctuations lead to dynamical correlations of particle multiplicity in momentum space. Studies of the correlation of the particle multiplicity in the transverse and longitudinal directions provide information on the particle production mechanism and the properties of the produced matter [1, 2, 3]. Studies of the multiplicity correlation in the transverse plane have revealed strong harmonic modulation of the particle densities in the azimuthal angle, commonly referred to as harmonic flow. The measurements of harmonic flow coefficients v_n [4, 5, 6, 7] and their EbyE fluctuations [8, 9, 10] have placed important constraints on the properties of the medium and transverse density fluctuations in the initial state.

The multiplicity correlations in the longitudinal direction are sensitive to the initial-state density fluctuations in pseudorapidity (η). These density fluctuations generate long-range correlations at the early stages of the collision, well before the onset of the collective flow, and appear as correlations of the multiplicity of produced particles separated in η . For example, EbyE differences between the number of nucleon participants in the target and the projectile, $N_{\text{part}}^{\text{F}}$ and $N_{\text{part}}^{\text{B}}$, may lead to a long-range asymmetry of the fireball [1, 11, 12]. In the wounded nucleon model, the fluctuations of the emission profile for each participant may lead to higher-order shape fluctuations in pseudorapidity [11]. Longitudinal multiplicity correlations can also be generated during the space-time evolution in the final state as resonance decay, jet fragmentation and Bose-Einstein correlations. These latter correlations are typically localized over a smaller range of η and are commonly referred to as short-range correlations.

Many previous studies are based on forward-backward (FB) correlations of particle multiplicity in two η ranges symmetric around the centre-of-mass of the collision system [13, 14]. A significant FB asymmetric component has been identified in proton-proton ($p+p$) [15, 16, 17, 18] and nucleus-nucleus (A+A) [19, 20] collisions. Recently, the study of multiplicity correlations has been generalized by decomposing the correlation function in each event into orthogonal polynomial functions, or more generally into principal components, each representing a unique component of the measured FB correlation [11, 21, 22]. The method has been applied to HIJING [23] and AMPT [24] models to extract different shape components of the multiplicity fluctuation.

The two-particle correlation function in pseudorapidity is defined as [14]:

$$C(\eta_1, \eta_2) = \frac{\langle N(\eta_1)N(\eta_2) \rangle}{\langle N(\eta_1) \rangle \langle N(\eta_2) \rangle} \equiv \langle R(\eta_1)R(\eta_2) \rangle, \quad R(\eta) \equiv \frac{N(\eta)}{\langle N(\eta) \rangle}, \quad (1)$$

where $N(\eta) \equiv dN/d\eta$ is the multiplicity density distribution in a single event and $\langle N(\eta) \rangle$ is the average distribution for a given event-centrality class. The correlation function is directly related to a single particle quantity $R(\eta)$, which characterizes the fluctuation of multiplicity relative to the average shape in a single event. In the absence of EbyE fluctuations, $R = C = 1$.

In principle, the correlation function should be defined in a narrow centrality interval, such that it contains only dynamical fluctuations that decouple from any residual centrality dependence in the average shape $\langle N(\eta) \rangle$, which would lead to a modulation of the projections of the correlation function along the η_1 or

η_2 axes. However, this effect can be removed by a simple redefinition of the correlation function [22]:

$$C_N(\eta_1, \eta_2) = \frac{C(\eta_1, \eta_2)}{C_p(\eta_1)C_p(\eta_2)}, \quad (2)$$

where

$$C_p(\eta_1) = \frac{\int C(\eta_1, \eta_2) d\eta_2}{2Y}, C_p(\eta_2) = \frac{\int C(\eta_1, \eta_2) d\eta_1}{2Y}, \quad (3)$$

are averages of the $C(\eta_1, \eta_2)$ along the η_2 or η_1 direction in the range $[-Y, Y]$. The resulting distribution is then renormalized such that the average value of $C_N(\eta_1, \eta_2)$ in the η_1 and η_2 plane is one.

Following the procedure of Refs. [11, 22], the correlation function is decomposed into orthogonal polynomials:

$$C_N(\eta_1, \eta_2) = 1 + \sum_{n,m=1}^{\infty} a_{n,m} \frac{T_n(\eta_1)T_m(\eta_2) + T_n(\eta_2)T_m(\eta_1)}{2}, \quad T_n(\eta) \equiv \sqrt{n + \frac{1}{2}} P_n(\eta/Y), \quad (4)$$

where the $P_0(x) = 1$, $P_1(x) = x$, $P_2(x) = (3x^2 - 1)/2, \dots$, are Legendre polynomials. The scale factors in $T_n(\eta)$ are chosen such that the $T_n(\eta)$ satisfy simple orthogonality and completeness relations:

$$\int_{-Y}^Y T_n(\eta) T_m(\eta) d\eta = \delta_{nm}, \quad \sum_{n=0}^{\infty} T_n(\eta_1) T_n(\eta_2) = \delta(\eta_1 - \eta_2). \quad (5)$$

The two-particle Legendre coefficients can be calculated directly from the measured correlation function:

$$a_{n,m} = \int C_N(\eta_1, \eta_2) \frac{T_n(\eta_1)T_m(\eta_2) + T_n(\eta_2)T_m(\eta_1)}{2} d\eta_1 d\eta_2. \quad (6)$$

According to Eq. 1, these coefficients can be directly related to the Legendre coefficients a_n for the single particle quantity $R(\eta)$:

$$a_{n,m} = \langle a_n a_m \rangle, \quad (7)$$

$$R(\eta) \propto 1 + \sum_n a_n T_n(\eta). \quad (8)$$

Therefore the two-particle correlation method measures, in effect, the root-mean-square (RMS) values of the EbyE a_n , $\sqrt{\langle a_n^2 \rangle}$, or the cross correlation between a_n and a_m , $\langle a_n a_m \rangle$.

Studies of the properties of $\langle a_n a_m \rangle$ have been carried out in the model framework [11, 22], and significant non-zero values have been shown for the first few terms. The first coefficient $\sqrt{\langle a_1^2 \rangle}$ is found to be associated with the asymmetry between N_{part}^F and N_{part}^B , while the second term reflects the EbyE fluctuation of the width of $N(\eta)$.

This note presents the first measurement of the two-dimensional (2-D) correlation function $C_N(\eta_1, \eta_2)$ over the pseudorapidity range of $|\eta| < 2.4$ in Pb+Pb collisions at a nucleon-nucleon centre-of-mass energy $\sqrt{s_{\text{NN}}} = 2.76$ TeV using the ATLAS detector at the LHC.¹ The correlation functions are measured for charged particles as a function of centrality and the associated coefficients $\langle a_n a_m \rangle$ are calculated.

¹ ATLAS uses a right-handed coordinate system with its origin at the nominal interaction point (IP) in the centre of the detector and the z -axis along the beam pipe. The x -axis points from the IP to the centre of the LHC ring, and the y -axis points upward. Cylindrical coordinates (r, ϕ) are used in the transverse plane, ϕ being the azimuthal angle around the beam pipe. The pseudorapidity is defined in terms of the polar angle θ as $\eta = -\ln \tan(\theta/2)$.

2 ATLAS detector and trigger

The ATLAS detector [25] provides nearly full solid-angle coverage of the collision point with tracking detectors, calorimeters and muon chambers. All of these are well suited for measurement of two-particle correlations over a large pseudorapidity range. This analysis primarily uses two subsystems: the inner detector (ID) and the forward calorimeter (FCal). The ID is contained within the 2 T field of a superconducting solenoid magnet and measures the trajectories of charged particles in the pseudorapidity range $|\eta| < 2.5$ and over the full azimuth. A charged particle passing through the ID traverses typically three modules of the silicon pixel detector (Pixel), four double-sided silicon strip modules of the semiconductor tracker (SCT), and a transition radiation tracker for $|\eta| < 2$. The FCal consists of three sampling layers, longitudinal in shower depth, and covers $3.2 < |\eta| < 4.9$. In heavy-ion collisions, the FCal is used mainly to measure the event centrality and event planes [26, 6].

The minimum-bias trigger used for this analysis requires signals in two zero-degree calorimeters (ZDC) or either of the two minimum-bias trigger scintillator (MBTS) counters. The ZDCs are positioned at ± 140 m from the collision point, detecting neutrons and photons with $|\eta| > 8.3$, and the MBTS covers $2.1 < |\eta| < 3.9$ on each side of the nominal interaction point. The ZDC trigger thresholds on each side are set below the peak corresponding to a single neutron. A timing requirement based on signals from each side of the MBTS is imposed to remove beam background.

3 Data Analysis

3.1 Event and track selection

This analysis is based on approximately $7 \mu\text{b}^{-1}$ of Pb+Pb data collected in 2010 at the LHC with a nucleon-nucleon centre-of-mass energy $\sqrt{s_{\text{NN}}} = 2.76$ TeV. The offline event selection requires a reconstructed primary vertex with longitudinal position $|z_{\text{vtx}}| < 100$ mm from the nominal centre of the ATLAS detector, as well as a time difference $|\Delta t| < 3$ ns between signals in the MBTS trigger counters on either side of the interaction point to suppress non-collision backgrounds. A coincidence between the signal in ZDCs at forward and backward pseudorapidity is required to reject a variety of background processes, while maintaining high efficiency for inelastic processes.

The Pb+Pb event centrality [27] is characterized using the total transverse energy (ΣE_{T}) deposited in the FCal over the pseudorapidity range $3.2 < |\eta| < 4.9$ at the electromagnetic energy scale [28]. From an analysis of the FCal ΣE_{T} distribution after all trigger and event-selection requirements, the fraction of the inelastic cross-section sampled is estimated to be $98 \pm 2\%$. The uncertainty associated with the centrality definition is evaluated by varying the effect of trigger and event-selection inefficiencies, as well as background rejection requirements, in the most peripheral FCal ΣE_{T} interval [27]. The FCal ΣE_{T} distribution is divided into a set of 5% percentile bins. A centrality interval refers to a percentile range, starting at 0% relative to the most central collisions. Thus the 0–5% centrality interval corresponds to the most central 5% of the events. A Monte Carlo Glauber analysis [29, 27] is used to estimate the average number of participating nucleons, N_{part} , for each centrality interval. These are summarized in Table 1. Following the convention of heavy-ion analyses, the centrality dependence of the results in this paper is presented as a function of N_{part} .

Table 1: The list of centrality intervals and associated values of the average number of participating nucleons N_{part} used in this analysis. The systematic uncertainties are taken from Ref. [27].

Centrality	0–5%	5–10%	10–15%	15–20%	20–25%	25–30%	30–35%	35–40%	40–45%
N_{part}	382 ± 2	330 ± 3	282 ± 4	240 ± 4	203 ± 4	170 ± 4	142 ± 4	117 ± 4	95 ± 4
Centrality	45–50%	50–55%	55–60%	60–65%	65–70%	70–75%	75–80%	80–85%	85–90%
N_{part}	76 ± 4	60 ± 3	46 ± 3	35 ± 3	25 ± 2	18 ± 2	12 ± 2	8.2 ± 1.2	5.4 ± 0.8

The multiplicity correlation function is measured using tracks in the ID that are required to have transverse momentum $p_T > 0.5$ GeV and $|\eta| < 2.4$. At least nine hits in the silicon detectors are required for each track, with no missing Pixel hits and not more than one missing SCT hit, taking into account the effects of known disabled modules. In addition, the point of closest approach of the track is required to be within 1 mm of the primary vertex in both the transverse and longitudinal directions [26]. The efficiency $\epsilon(\eta, p_T)$ of the track reconstruction and track selection requirements is evaluated using simulated Pb+Pb events produced with the HIJING event generator (version 1.38b) [23]. The response of the detector is simulated using GEANT4 [30, 31] and the resulting events are reconstructed with the same algorithms that are applied to the data. The absolute efficiency increases by 7% for p_T between 0.5 GeV and 0.8 GeV and varies only weakly for $p_T > 0.8$ GeV. However, the efficiency varies more strongly with η and event multiplicity [26]. For $p_T > 0.8$ GeV, it ranges from 72% at $\eta \approx 0$ to 57% for $|\eta| > 2$ in peripheral collisions, while it ranges from 72% at $\eta \approx 0$ to about 42% for $|\eta| > 2$ in central collisions. As the reconstruction efficiency and acceptance of the ID shifts slightly in η with changing z_{vtx} , the efficiency is calculated separately for events in different z_{vtx} intervals in steps of 10 mm.

3.2 Two-particle correlations

Previously ATLAS has published measurements of the two-particle correlations in relative azimuthal angle ($\phi_1 - \phi_2$) and relative pseudorapidity ($\eta_1 - \eta_2$) using the same dataset [6, 8, 10]. The two-particle correlation analysis presented in this note follows a similar procedure, except that the measurement is performed differentially in η_1 and η_2 . Charged particles measured by the ID over $|\eta| < Y = 2.4$ are used for constructing the correlation function.

The two-particle correlation function defined in Eq. 1 is constructed as the ratio of distributions for same-event pairs (or foreground pairs $S(\eta_1, \eta_2) \propto \langle N(\eta_1)N(\eta_2) \rangle$) and mixed-event pairs (or background pairs $B(\eta_1, \eta_2) \propto \langle N(\eta_1) \rangle \langle N(\eta_2) \rangle$):

$$C(\eta_1, \eta_2) = \frac{S(\eta_1, \eta_2)}{B(\eta_1, \eta_2)}. \quad (9)$$

The mixed-event pair distribution is constructed by combining tracks from the foreground event with another event with similar event centrality based on FCal ΣE_T (matched within 0.5%) and z_{vtx} (matched within 2.5 mm). The events are also required to be close to each other in time to account for possible time-dependent variation of the detector conditions. The mixed-event distribution accounts properly for detector inefficiencies and non-uniformity, but contains no physical correlations. The normalization of $C(\eta_1, \eta_2)$ is chosen such that its average value in the η_1 – η_2 plane is one. Due to the required symmetry of $C(\eta_1, \eta_2) = C(\eta_2, \eta_1)$ and, for a symmetric collision system, $C(\eta_1, \eta_2) = C(-\eta_1, -\eta_2)$, pairs are filled in one quadrant of the (η_1, η_2) space defined by $\eta_1 - \eta_2 > 0$ and $\eta_1 + \eta_2 > 0$ and then reflected to the other quadrants. To correct $S(\eta_1, \eta_2)$ and $B(\eta_1, \eta_2)$ for the individual inefficiencies of particles in the pair, the pairs are weighted by the inverse product of their track reconstruction efficiencies $1/(\epsilon_1 \epsilon_2)$. Remaining

detector distortions not accounted for by the reconstruction efficiency largely cancel in the same-event to mixed-event ratio.

The shape of the single-particle multiplicity distribution and track reconstruction efficiency vary with event centrality, and therefore the distribution of $\langle N(\eta) \rangle$ also varies with event centrality. Due to the finite resolution of the FCal in determining the centrality, the two events used to construct the mixed-event pairs may have slightly different event activity from the foreground event, and hence they may have slightly different shapes in $\langle N(\eta) \rangle$. This mismatch leads to a small modulation of the correlation function along the η_1 direction and another along the η_2 direction. This residual single-particle centrality dependence is removed by projecting the correlation function on to η_1 or η_2 axes and dividing out from the original correlation function via Eq. 2. The new correlation function $C_N(\eta_1, \eta_2)$, defined in Eq. 3, is then renormalized such that its average value in the η_1 – η_2 plane is one. This correlation function also satisfies the same two symmetry constraints as the original correlation function:

$$C_N(\eta_1, \eta_2) = C_N(\eta_2, \eta_1), \quad (10)$$

$$C_N(\eta_1, \eta_2) = C_N(-\eta_1, -\eta_2). \quad (11)$$

As an alternative to using centrality determined from FCal ΣE_T to select the matching event for the mixed-events, mixed-event pairs can be formed from events that are matched in a very narrow range of total reconstructed tracks $N_{\text{ch}}^{\text{rec}}$ for $p_T > 0.5$ GeV. In this case, events are divided into two hundred $N_{\text{ch}}^{\text{rec}}$ ranges each containing 0.5% of the statistics, and the two events used to construct $B(\eta_1, \eta_2)$ are required to belong to the same $N_{\text{ch}}^{\text{rec}}$ range, in addition to the z_{vtx} matching requirement.

Figure 1 shows the correlation functions calculated in the 35–40% centrality interval for these two event-mixing schemes. The top panels show results for mixed-events obtained in narrow $N_{\text{ch}}^{\text{rec}}$ bins, while the bottom panels show results when mixed-events are obtained in narrow ΣE_T bins. The original correlation functions have rather different shapes. However, after dividing out the projections as per Eq. 2, the resulting correlation functions $C_N(\eta_1, \eta_2)$, as shown in the right column, are nearly identical to each other. This implies that the difference between the two $C(\eta_1, \eta_2)$ distributions is indeed due to residual centrality dependence. This residual centrality dependence is larger for the ΣE_T -binned case, since the events in each narrow ΣE_T range still span a large interval in $N_{\text{ch}}^{\text{rec}}$ (see Fig. 12 in Appendix). The results presented in this note are obtained using the $N_{\text{ch}}^{\text{rec}}$ -based event-mixing scheme.

3.3 Extraction of the Legendre coefficients associated with longitudinal multiplicity fluctuations

In the azimuthal correlation analysis, the azimuthal structure of the correlation function is characterized by harmonic coefficients v_n obtained via a Fourier decomposition [32, 6]. A similar approach can be applied for pseudorapidity correlation [11, 22]. Following Eq. 4, the correlation functions are expanded into Legendre polynomial functions, and the two-particle Legendre coefficients $\langle a_n a_m \rangle$ are calculated directly from the correlation function according to Eq. 6. The two-particle correlation method measures, in effect, the RMS values of the event-by-event a_n . Therefore, the final results on the coefficients are presented in terms of $\sqrt{|\langle a_n a_m \rangle|}$. As a consequence of the condition for a symmetric collision system (Eq. 11), the odd and even coefficients should be uncorrelated:

$$a_{n,n+1} = \langle a_n a_{n+1} \rangle = 0. \quad (12)$$

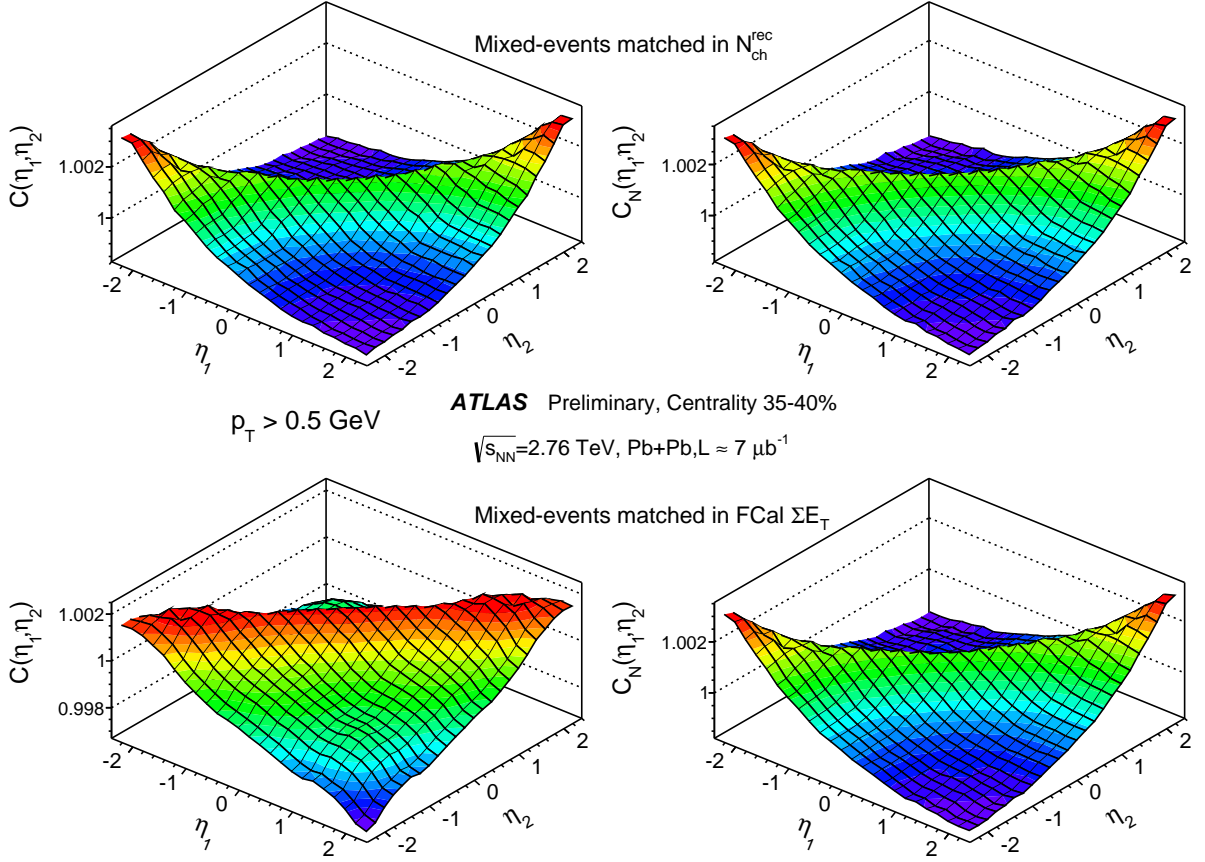


Figure 1: The correlation functions $C(\eta_1, \eta_2)$ (left panels) and $C_N(\eta_1, \eta_2)$ (right panels). The mixed-event pairs are obtained by matching two events in either narrow N_{ch}^{rec} intervals (top panels) or narrow FCal ΣE_T intervals (bottom panels), where N_{ch}^{rec} is the total reconstructed tracks for $p_T > 0.5$ GeV and ΣE_T is the total transverse energy deposited in the FCal over the pseudorapidity range $3.2 < |\eta| < 4.9$. These correlation functions are obtained for the 35–40% centrality interval.

The shape of the first three Legendre bases in 2-D are shown in Fig. 2. The first base function has the shape of $\eta_1 \eta_2$ and is directly sensitive to the FB asymmetry of the EbyE fluctuation. The second base has a quadratic shape in the η_1 and η_2 directions and is sensitive to the EbyE fluctuation in the width of the $N(\eta)$ distribution. Keeping only the first term, the shape of the correlation function can be approximated by:

$$C_N(\eta_1, \eta_2) \sim 1 + \langle a_1^2 \rangle \frac{3}{2Y^2} \eta_1 \eta_2, \quad (13)$$

with $Y = 2.4$. Expressed in terms of two new orthogonal variables: $\eta_- = \eta_1 - \eta_2 \equiv \Delta\eta$ and $\eta_+ = \eta_1 + \eta_2$, the correlation function can be approximated by [11]:

$$C_N(\eta_-, \eta_+) \sim 1 + \langle a_1^2 \rangle \frac{3}{8Y^2} (\eta_+^2 - \eta_-^2) \approx 1 + 0.065 \langle a_1^2 \rangle (\eta_+^2 - \eta_-^2). \quad (14)$$

Therefore a quadratic shape is expected along the diagonal directions of the correlation function if the a_1 component dominates. In general, the contribution of a given component can be estimated from the projection of $C_N(\eta_1, \eta_2)$ along a direction that maximizes the strength of the desired component.

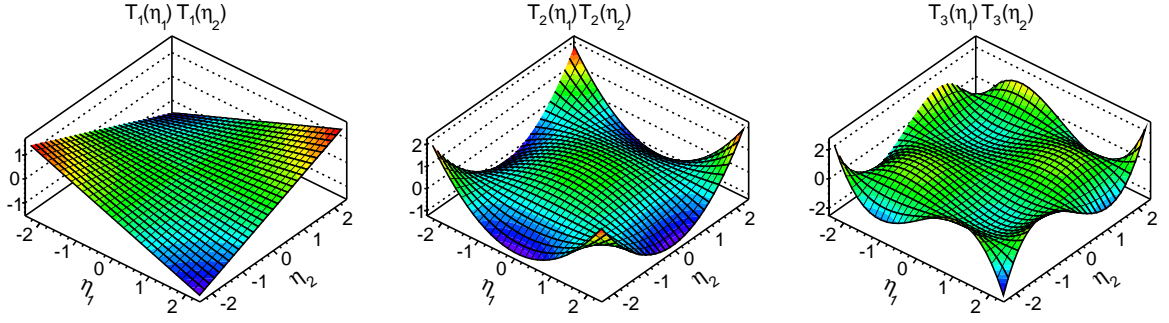


Figure 2: The shape of the first three Legendre bases associated with $a_{1,1}$, $a_{2,2}$ and $a_{3,3}$ in the two-particle correlation function.

3.4 Systematic uncertainties

The systematic uncertainties in this analysis arise from the event-mixing scheme, reconstruction efficiency, pair acceptance, and consistency of correlation functions between reconstructed tracks and generated charged particles in simulated events. Each source is discussed separately below.

The correlation function relies on the mixed-event pair distribution to reproduce detector acceptance effects in the signal distribution. A natural way of quantifying the influence of residual detector effects is to calculate $C_N(\eta_1, \eta_2)$ under a different condition, and then construct the ratio to the default condition: $r(\eta_1, \eta_2)$. The average deviation of $r(\eta_1, \eta_2)$ from unity can be compared with the correlation signal to estimate the systematic uncertainties on the correlation function. The same $r(\eta_1, \eta_2)$ distribution can also be expanded in a Legendre series and the resulting coefficients $a_{n,m}^r$ can be used to estimate the systematic uncertainties for the Legendre coefficients. For most systematic variations, the fractional uncertainty is largest in central collisions and smaller for more peripheral collisions.

Uncertainties due to the event-mixing scheme are evaluated by varying the criteria for matching events in centrality and z_{vtx} . The $a_{n,m}^r$ values are calculated for each case. The uncertainty from variation of the matching range in z_{vtx} is less than 3% of the correlation signal and 1–7% for $\sqrt{\langle a_n^2 \rangle}$. The sensitivity of results to the matching range in centrality is studied by matching events in $N_{\text{ch}}^{\text{rec}}$ or FCal ΣE_T . In each case, the bin size in $N_{\text{ch}}^{\text{rec}}$ or ΣE_T for event matching is varied such that the event statistics in each bin changes from 0.3% to 1%. Most of the changes appear as modulations of the projections of the correlation function in η_1 or η_2 as defined in Eq. 3, and the renormalized correlation function $C_N(\eta_1, \eta_2)$ is very stable. The difference between different variations and between the two event-mixing schemes amounts to at most 2% of the correlation signal and 0.5–8% change in $\sqrt{\langle a_n^2 \rangle}$. The analysis is also repeated separately for events with $|z_{\text{vtx}}| < 50$ mm and $50 < |z_{\text{vtx}}| < 100$ mm. Good consistency is seen for $\sqrt{\langle a_1^2 \rangle}$ and $\sqrt{\langle a_2^2 \rangle}$ in most centrality intervals, and 1–9% differences are observed for $\sqrt{\langle a_3^2 \rangle}$ and $\sqrt{-\langle a_1 a_3 \rangle}$, and these are included in the final uncertainties. To evaluate the stability of the correlation function, the entire dataset is divided into 17 periods, and the correlation function and a_n coefficients are calculated for each group. The results are found to be consistent within 3% for $\sqrt{\langle a_1^2 \rangle}$ and $\sqrt{\langle a_2^2 \rangle}$, with larger differences for higher-order coefficients.

The shape of the correlation function is not very sensitive to the uncertainty on the tracking efficiency correction, since this correction is applied in both numerator and denominator. On the other hand, both the

correlation signal and reconstruction efficiency are observed to increase with p_T , and hence the correlation signal and associated $\langle a_n a_m \rangle$ coefficients are expected to be smaller when the reconstruction efficiency is applied. Indeed, a 3–5% decrease in $\sqrt{\langle a_n^2 \rangle}$ is observed after applying this correction. However, the actual change of the results associated with uncertainty in the reconstruction efficiency is found to be smaller. This uncertainty is estimated by varying the track selection criteria in the simulation, re-analyzing the data using corresponding efficiencies and evaluating the change in the signal. As the reconstruction efficiency and acceptance of the ID shift slightly in η with changing z_{vtx} , the efficiency has been evaluated and applied separately in 10 mm z_{vtx} steps. The uncertainty associated with this correction is evaluated by varying the width of the z_{vtx} steps. The total uncertainty from these sources amounts to less than 4% for $\sqrt{\langle a_1^2 \rangle}$ and less than 7% for $\sqrt{\langle a_2^2 \rangle}$ and $\sqrt{\langle a_3^2 \rangle}$ in most central collisions, and decreases to less than 2% in mid-central and peripheral collisions.

The reconstruction efficiency has been assumed to be independent for the two tracks in the pair. However, track splitting (the signal produced by one particle is reconstructed incorrectly as two) and track merging (reconstructing one track instead of two) can lead to additional structures in the two-particle correlations. These structures are observed to concentrate at small $\Delta\eta$ and $\Delta\phi$ ($|\Delta\eta| \lesssim 0.02$ and $|\Delta\phi| \lesssim 0.1$), and they are reasonably described in the HIJING simulation. In order to evaluate the impact of these very short-range structures, the analysis is repeated by excluding $|\Delta\eta| < 0.02$. The difference from the default result is less than 1% in most cases and increases to 1–7% in the most central collisions, depending on the order of the coefficients.

The correlation function $C_N(\eta_1, \eta_2)$ has some small localized structures that are beyond the statistical fluctuations. These structures are due to residual detector effects in the pair acceptance that are not removed by the event-mixing procedure, which can be important for extraction of the higher-order coefficients. Indeed, the Legendre coefficients for $n \geq 8$ show significant non-statistical fluctuations around zero. Therefore, the spread of $\langle a_n^2 \rangle$ for $n \geq 10$ and $\langle a_n a_{n+2} \rangle$ for $n \geq 8$ are quoted as uncertainty for a_n . This uncertainty is about 1×10^{-5} for $\langle a_n a_m \rangle$ in most central collisions and increases to 4×10^{-4} in the most peripheral collisions.

The HIJING events used for evaluating the reconstruction efficiency have a significant correlation signal and sizable a_n coefficients. The correlation function and a_n values obtained using the reconstructed tracks are compared with those obtained using the generated charged particles. The differences are taken as an estimate of the systematic uncertainties. These differences are found to be a few percent or less in most cases: the maximum difference is found to be 9% for a_1 (around mid-centrality), and 5% for a_2 and a_3 . The higher-order coefficients are found to be consistent with each other within the statistical uncertainty of the HIJING sample.

The different sources of systematic uncertainties described above are added in quadrature to give the total systematic uncertainties for the correlation function and RMS values for a_n , which are summarized in Tables 2 and 3, respectively. The systematic uncertainty quoted for each source usually covers the maximum uncertainty in the specified centrality interval.

Table 2: Summary of average systematic uncertainties in percent for the 2-D correlation function. The uncertainty is calculated as the variation averaged over the entire η_1 and η_2 space relative to the observed strength of the correlation signal defined as the difference between maximum and minimum.

Centrality	0–20%	20–40%	40–60%	60–90%
Event-mixing [%]	2–4	1–2	0.5–1.0	0.7–1.4
Run-by-run stability [%]	2–3	1–2	0.9	1–1.5
z_{vtx} variation [%]	1.5–3	1–1.6	0.9	1.0
Track selection & efficiency [%]	1.4–2.8	0.5–1	0.4	0.4–0.8
Pair cuts [%]	0.8–2	0.4–0.8	<0.3	<0.2
Simulation consistency [%]	3–5	1.5–3	1–1.5	1–1.5
Total [%]	5.5–8.5	2.5–4	2	2–3.5

Table 3: Summary of systematic uncertainties in percent for $\sqrt{\langle a_1^2 \rangle}$, $\sqrt{\langle a_2^2 \rangle}$, $\sqrt{\langle a_3^2 \rangle}$ and $\sqrt{-\langle a_1 a_3 \rangle}$.

	Uncertainty in $\sqrt{\langle a_1^2 \rangle}$				Uncertainty in $\sqrt{\langle a_2^2 \rangle}$			
Centrality	0–20%	20–40%	40–60%	60–90%	0–20%	20–40%	40–60%	60–90%
Event-mixing [%]	1.5–3	1–1.5	1	1–4	4–7	2.5–3.7	1.6–2.3	1–4
Run-by-run stability [%]	0.7–1.6	0.7–1	0.5	0.5–1.5	2–3	1–2	1.0	1–3
z_{vtx} variation [%]	0.5–1.5	0.5–1.3	0.8	0.5–1.0	1–6	1–4	1–2.2	1
Track selec.& efficiency[%]	1.6–4.3	0.6–1.1	0.5	0.5	1–6	1	1	1–2
Pair cuts [%]	0.4–1	0.5	<0.2	<0.2	0.4–2	0.5	<0.2	<0.2
Pair acceptance [%]	1.4–1.8	0.7–1.2	0.5–0.7	0.2–0.5	4–5.5	2–3.5	1.3–2.0	0.4–1.3
Simulation consistency [%]	2–10	4–7	1–1.6	3–8	2–5	2–4	1–3	2–10
Total [%]	4–11	4–8	2	3–9	8.5–10	4–6	3–5	3–10

	Uncertainty in $\sqrt{\langle a_3^2 \rangle}$				Uncertainty in $\sqrt{-\langle a_1 a_3 \rangle}$			
Centrality	0–20%	20–40%	40–60%	60–90%	0–20%	20–40%	40–60%	60–90%
Event-mixing [%]	8–12	4.3–7.6	2.4–3.4	1–4	1–1.6	1	0.7–1	1–4
Run-by-run stability [%]	4–7	3–5	2–2.5	2–5	3–6	2–4	3–4	3–6
z_{vtx} variation [%]	3–9	2–5	1–4	1–3	3–5	3–4	2–3	1–2
Track selec.& efficiency[%]	2–7	1–2	1	1	1.5–7	1–2	1–2	1–3
Pair cuts [%]	1–7	0.5–1	<0.5	<0.5	3–5	1–3	0.5–1	<0.5
Pair acceptance [%]	8.5–12	3.5–7	2–3.6	0.6–2.1	7.3–10.5	5–8.5	3.5–5.5	1.4–4
Simulation consistency [%]	1.6–4	1–5	2–3	2–10	3–7	1–4	1–6	2–7
Total [%]	13–18	6–12	3.5–6.5	4–11	11–14	7–10	5–8	5–11

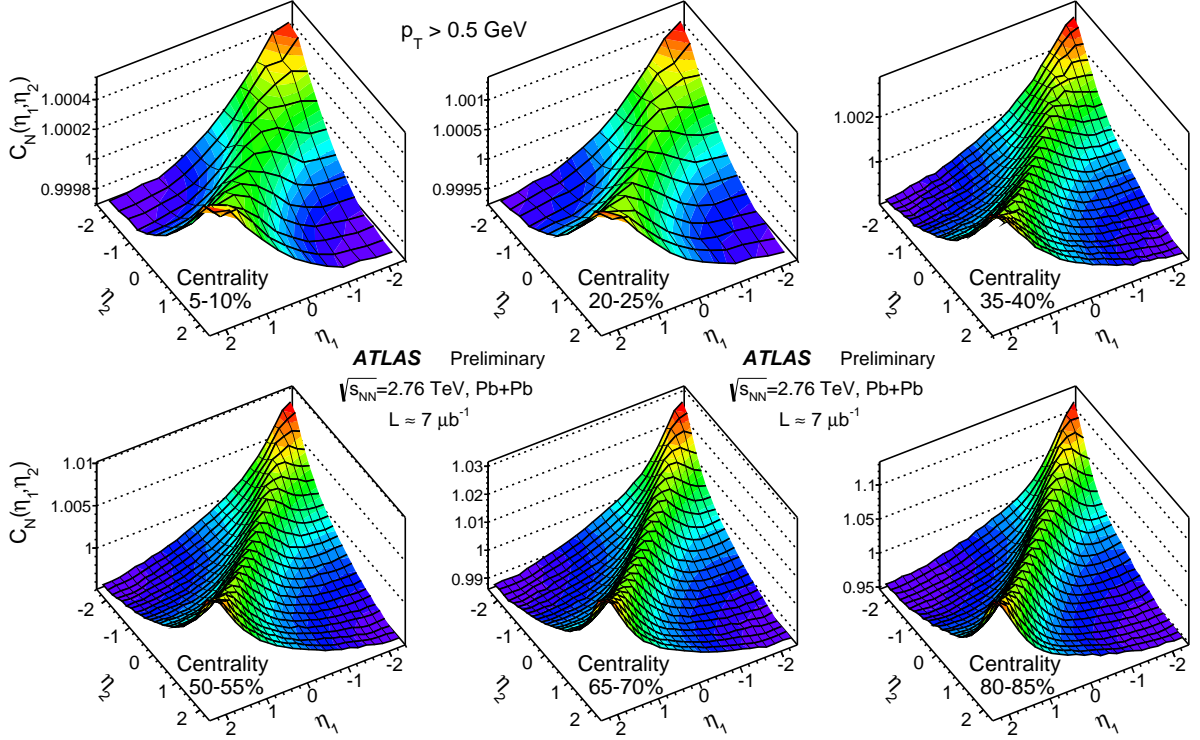


Figure 3: The 2-D pseudorapidity correlation function $C_N(\eta_1, \eta_2)$ in six centrality intervals.

4 Results

4.1 Correlation functions

Figure 3 shows the correlation function $C_N(\eta_1, \eta_2)$ in six centrality intervals. These correlation functions show a broad “ridge-like” shape along $\eta_1 = \eta_2$ (or $\eta_- \approx 0$), and a depletion at around $\eta_1 = -\eta_2 \approx \pm 2.4$ (or $\eta_+ \approx 0$ and $\eta_1 \approx \pm 2.4$). The magnitude of the ridge increases towards large η_+ and from central to peripheral collisions, while the width of the ridge narrows slightly from central to peripheral collisions. This narrowing trend could reflect significant contributions from short-range correlation sources, such as resonance decays, jet fragmentation and Bose-Einstein correlations, which become more significant in the peripheral collisions.

To analyse the shape of the correlation function in more detail, the correlation function is expressed in terms of η_- and η_+ . The resulting correlation function $C_N(\eta_-, \eta_+)$ is then projected onto the η_- (η_+) axis in narrow ranges of η_+ (η_-). These projections, $C_N(\eta_-)$ or $C_N(\eta_+)$, are shown in Figs. 4 and 5 for several centrality intervals. These projections allow a qualitative separation of the short-range correlation effects centred around $\eta_- \approx 0$ from the genuine long-range correlations. The traditional FB correlation analysis probes mostly $C_N(\eta_-)$ in the slice of η_+ around 0. In contrast, this analysis provides more detailed information on the multiplicity correlation by exploring the correlation structures in the full pseudorapidity phase space.

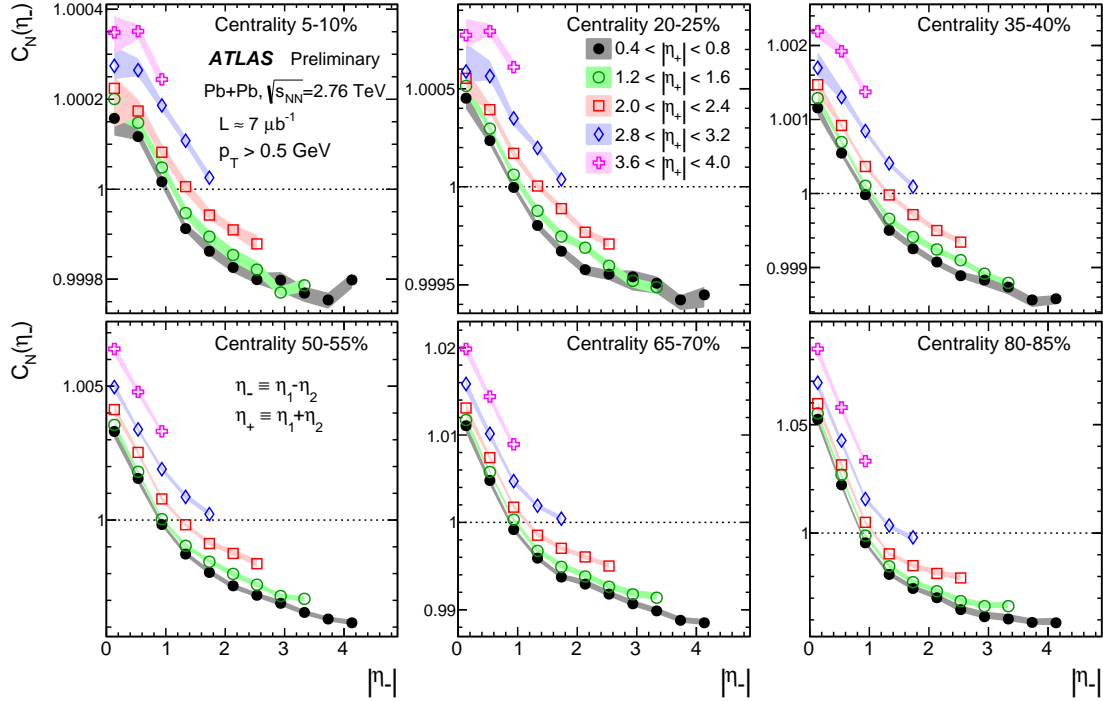


Figure 4: The 1-D correlation functions $C(\eta_-)$ with $\eta_- \equiv \eta_1 - \eta_2$ obtained by projecting the $C_N(\eta_1, \eta_2)$ in five narrow ranges of $\eta_+ \equiv \eta_1 + \eta_2$ indicated by the figure legend. Each panel represents results from one centrality interval. The shaded bands are the total uncertainties.

Along the η_- direction, the correlation functions in Fig. 4 all peak at $\eta_- = 0$ and decrease quickly for $|\eta_-| < 1$, followed by a much weaker decrease beyond that. The initial rapid decrease is consistent with the dominance of short-range correlations, which are mostly centred around $\eta_- \approx 0$, and the weaker decrease at large $|\eta_-|$ could be related to the $-\eta_-^2$ term in Eq. 14. In Fig. 5, the correlation functions along the η_+ direction show a clear quadratic shape in all η_- slices, consistent with the η_+^2 term in Eq. 14 associated with the a_1 component. This would be the case if the strength of the short-range correlations changes slowly along the η_+ direction.

To quantify this quadratic dependence, the $C_N(\eta_+)$ data shown in Fig. 5 are fit to a function motivated by Eq. 14 for each η_- range:

$$C_N(\eta_+) = 0.065 \langle a_1^2 \rangle \eta_+^2 + b, \quad (15)$$

where b is a constant. The fits are performed for distributions that have more than five data points. The quality of the fits is generally very good, and the extracted coefficients $\sqrt{\langle a_1^2 \rangle}_{\text{Fit}}$ together with the total uncertainties are shown in Fig. 6. For the 0–40% centrality range, $\sqrt{\langle a_1^2 \rangle}_{\text{Fit}}$ values increase slightly with η_- and then remain flat for $|\eta_-| > 1.5$. This weak dependence is due either to the influence of the short-range correlations or to contributions from higher-order Legendre components. The value of $\sqrt{\langle a_1^2 \rangle}_{\text{Fit}}$ increases rapidly with centrality: it increases from ~ 0.015 in the 0–5% centrality interval to ~ 0.05 in the 50–55% centrality interval to ~ 0.2 in the 80–85% centrality interval.

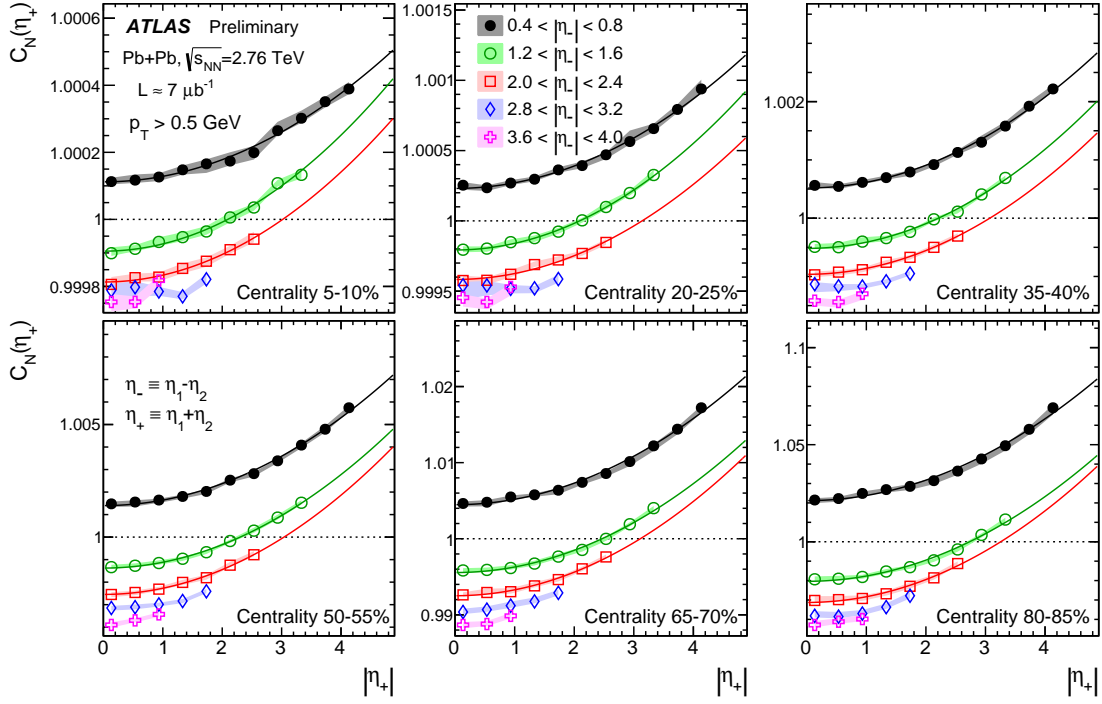


Figure 5: The 1-D correlation functions $C(\eta_+)$ with $\eta_+ \equiv \eta_1 + \eta_2$ obtained by projecting the $C_N(\eta_1, \eta_2)$ in five narrow ranges of $\eta_- \equiv \eta_1 - \eta_2$ indicated by the figure legend. The solid curves indicate the fits to Eq. 15. Each panel represents results from one centrality interval. The shaded bands are the total uncertainties.

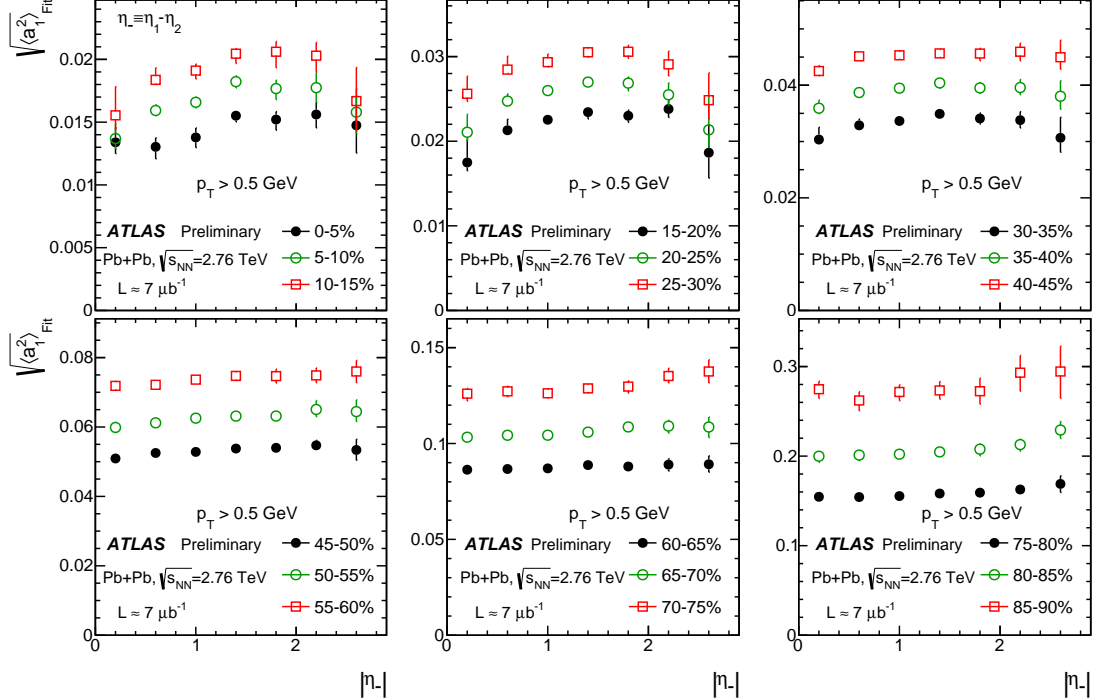


Figure 6: The value of $\sqrt{\langle a_1^2 \rangle}_{\text{Fit}}$ from fit to $C_N(\eta_+)$ via Eq. 15 as a function of $|\eta_-|$ for different centrality intervals. The error bars are the total uncertainties.

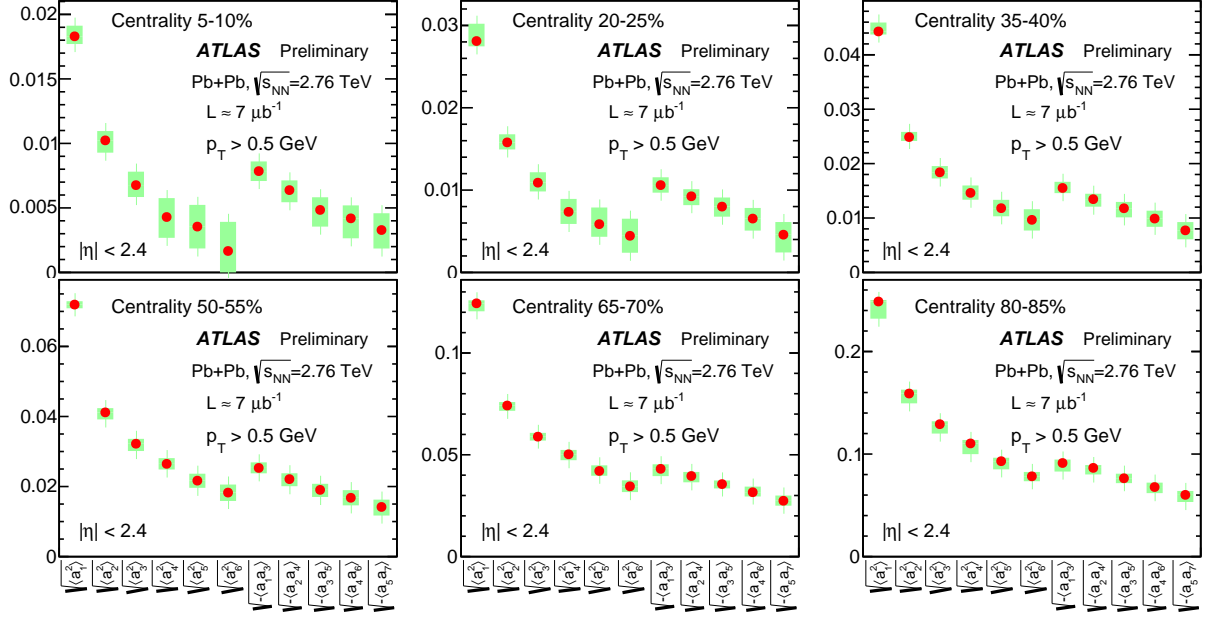


Figure 7: The Legendre spectrum $\sqrt{\langle a_n^2 \rangle}$ and $\sqrt{-\langle a_n a_{n+2} \rangle}$ calculated via Eq. 6 from 2-D correlation functions. The shaded bands are the total uncertainties.

4.2 Legendre coefficients from the correlation function

Using Eq. 6, the Legendre coefficients are calculated directly from the 2-D correlation functions. The RMS values of the first six significant coefficients are obtained and shown for six centrality intervals in Fig. 7. The $\sqrt{\langle a_n^2 \rangle}$ coefficients are largest for $n = 1$ and decrease quickly with increasing n . Significant mixed coefficients $\langle a_n a_m \rangle$ are also observed. The most significant group of mixed coefficients $\langle a_n a_{n+2} \rangle$ is found to be negative, implying that a_n and a_{n+2} are generally anti-correlated. The first five mixed terms are shown as $\sqrt{-\langle a_n a_{n+2} \rangle}$ ($n = 1-5$) in Fig. 7.

Figure 8 shows the centrality dependence (in terms of N_{part}) of $\sqrt{\langle a_1^2 \rangle}$, $\sqrt{\langle a_2^2 \rangle}$, $\sqrt{\langle a_3^2 \rangle}$ and the leading mixed term $\sqrt{-\langle a_1 a_3 \rangle}$. All coefficients increase strongly with decreasing N_{part} . This increase reflects the contribution from both short-range and genuine long-range correlations. In Figure 9, these coefficients are compared to those from the HIJING model prediction for Pb+Pb collisions at the same collision energy. The $\sqrt{\langle a_n^2 \rangle}$ values from the HIJING model have a weak dependence on n , and they are systematically larger than the data, except in the most peripheral collisions.

Figure 10 compares the $\sqrt{\langle a_1^2 \rangle}$ values calculated directly from the 2-D correlation function with those obtained from the fits in several $|\eta_-|$ ranges as shown in Fig. 5. The values from the fits are always smaller than those from direct calculation by 2–20% depending on the centrality interval and the choice of $|\eta_-|$ range. These results are also related to the RMS value of the asymmetry between the number of participating nucleons in the forward-going and backward-going nucleus, $N_{\text{part}}^{\text{F}}$ and $N_{\text{part}}^{\text{B}}$, respectively [22]:

$$A_{N_{\text{part}}} = \frac{N_{\text{part}}^{\text{F}} - N_{\text{part}}^{\text{B}}}{N_{\text{part}}^{\text{F}} + N_{\text{part}}^{\text{B}}}. \quad (16)$$

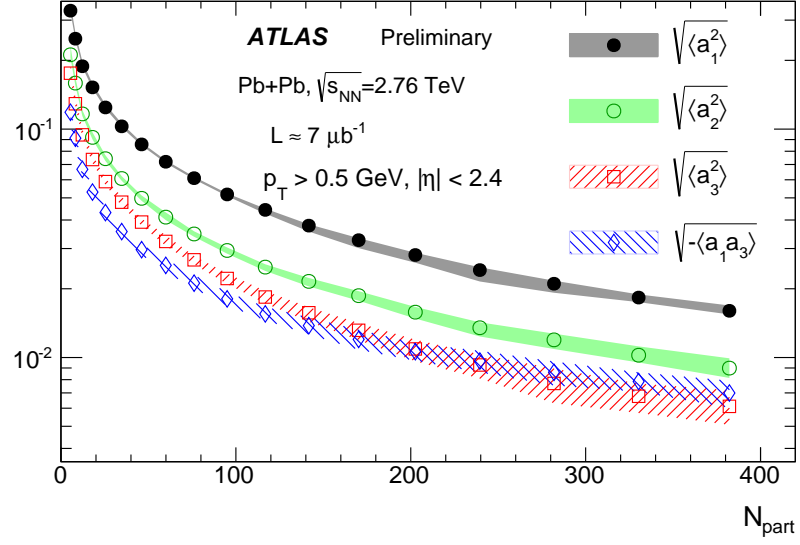


Figure 8: The centrality (in terms of total number of participating nucleons N_{part}) dependence of four Legendre coefficients: $\sqrt{\langle a_1^2 \rangle}$, $\sqrt{\langle a_2^2 \rangle}$, $\sqrt{\langle a_3^2 \rangle}$ and $\sqrt{-\langle a_1 a_3 \rangle}$. The shaded bands are the total uncertainties.

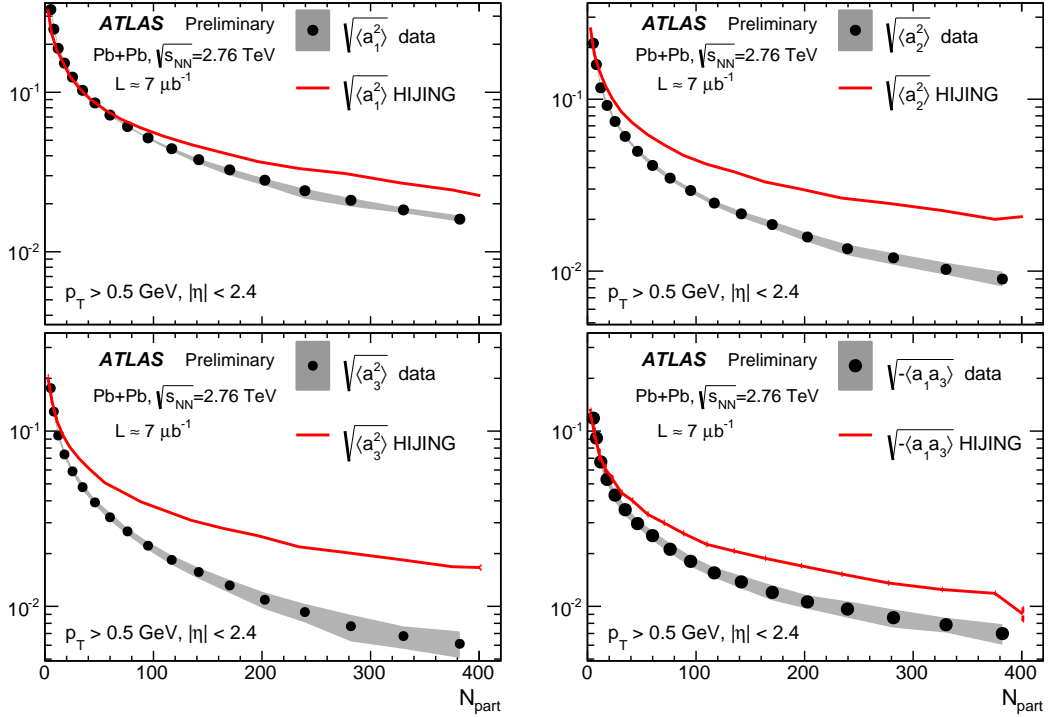


Figure 9: The centrality (in terms of total number of participating nucleons N_{part}) dependence of four Legendre coefficients: $\sqrt{\langle a_1^2 \rangle}$, $\sqrt{\langle a_2^2 \rangle}$, $\sqrt{\langle a_3^2 \rangle}$ and $\sqrt{-\langle a_1 a_3 \rangle}$, compared to the HIJING model. The shaded bands are the total uncertainties.

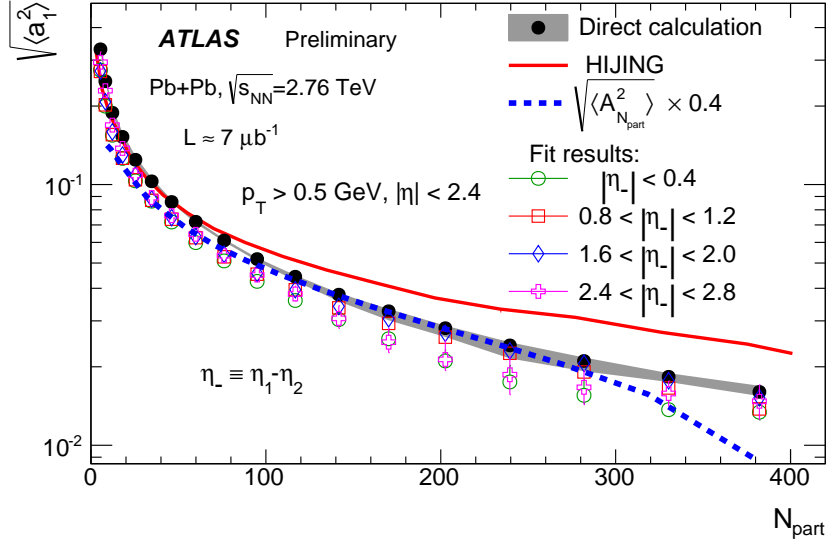


Figure 10: The centrality (in terms of total number of participating nucleons N_{part}) dependence of $\sqrt{\langle a_1^2 \rangle}$ calculated directly from the $C_N(\eta_1, \eta_2)$ (solid circles), those obtained from fits shown in Fig. 5 (open symbols), HIJING model prediction (solid line), as well as the RMS values of $A_{N_{\text{part}}}$ from Eq. 16 (dashed line). The shaded bands or error bars are the total uncertainties.

This asymmetry is calculated event-by-event from the Glauber model [29], and its RMS values $\sqrt{\langle A_{N_{\text{part}}}^2 \rangle}$ are scaled down by an arbitrary factor of 0.4 to match approximately the values of $\sqrt{\langle a_1^2 \rangle}$ as shown in Fig. 10. Comparing to $\sqrt{\langle a_1^2 \rangle}$, the values for $\sqrt{\langle A_{N_{\text{part}}}^2 \rangle}$ show a stronger decrease toward most central collisions and a slightly weaker increase toward most peripheral collisions.

5 Summary

Two-particle pseudorapidity correlations are measured in $\sqrt{s_{\text{NN}}} = 2.76$ TeV Pb+Pb collisions with a total integrated luminosity of approximately $7 \mu\text{b}^{-1}$ using the ATLAS detector at the LHC. The correlation functions $C_N(\eta_1, \eta_2)$ are obtained as a function of centrality for charged particles with $p_T > 0.5$ GeV and over the pseudorapidity range $-2.4 < \eta_1, \eta_2 < 2.4$ for the two particles. The correlation function shows enhancement along the $\eta_1 \approx \eta_2$ direction and suppression at $\eta_1 \approx -\eta_2 \sim \pm 2.4$, consistent with the expectation from an event-by-event forward-backward asymmetry in the multiplicity fluctuation. These structures are further investigated by projecting the 2-D correlation function in narrow ranges of $\eta_- = \eta_1 - \eta_2$ and $\eta_+ = \eta_1 + \eta_2$. The $C_N(\eta_-)$ distribution shows a clear quadratic dependence, characteristic of forward-backward asymmetry induced by the asymmetry in the number of participating nucleons in the two colliding nuclei.

The correlation function is decomposed into a sum of products of Legendre polynomials that describe the different shape components, and the coefficients $\langle a_n a_m \rangle$ are calculated. Significant values are observed for $\langle a_n^2 \rangle$ and $\langle a_n a_{n+2} \rangle$, which decrease quickly with increasing n . These coefficients are observed

to increase for peripheral collisions, consistent with the increase of the multiplicity fluctuation for smaller collision systems. The leading coefficient a_1 is compared to those obtained from fits to $C_N(\eta_+)$, as well as to the asymmetry between the number of participating nucleons in the two colliding nuclei. These quantities all show similar shapes in their centrality dependence. The fit results are 2–20% smaller than that obtained from a Legendre expansion, which could be due to the stronger influence of short-range correlations on the a_1 calculated directly from the Legendre expansion.

References

- [1] A. Bialas, A. Bzdak, and K. Zalewski, *Phys. Lett. B* **710** (2012) 332, [arXiv:1107.1215 \[hep-ph\]](#).
- [2] P. Bozek, W. Broniowski, and J. Moreira, *Phys. Rev. C* **83** (2011) 034911, [arXiv:1011.3354 \[nucl-th\]](#).
- [3] J. Jia, *J. Phys. G* **41** (2014) 124003, [arXiv:1407.6057 \[nucl-ex\]](#).
- [4] PHENIX Collaboration, A. Adare et al., *Phys. Rev. Lett.* **107** (2011) 252301, [arXiv:1105.3928 \[nucl-ex\]](#).
- [5] ALICE Collaboration, K. Aamodt et al., *Phys. Rev. Lett.* **107** (2011) 032301, [arXiv:1105.3865 \[nucl-ex\]](#).
- [6] ATLAS Collaboration, *Phys. Rev. C* **86** (2012) 014907, [arXiv:1203.3087 \[hep-ex\]](#).
- [7] CMS Collaboration, *Phys. Rev. C* **89** (2014) 044906, [arXiv:1310.8651 \[nucl-ex\]](#).
- [8] ATLAS Collaboration, *JHEP* **1311** (2013) 183, [arXiv:1305.2942 \[hep-ex\]](#).
- [9] ATLAS Collaboration, *Phys. Rev. C* **90** (2014) 024905, [arXiv:1403.0489 \[hep-ex\]](#).
- [10] ATLAS Collaboration, [arXiv:1504.01289 \[hep-ex\]](#).
- [11] A. Bzdak and D. Teaney, *Phys. Rev. C* **87** (2013) 024906, [arXiv:1210.1965 \[nucl-th\]](#).
- [12] J. Jia and P. Huo, *Phys. Rev. C* **90** (2014) 034915, [arXiv:1403.6077 \[nucl-th\]](#).
- [13] A. Bialas and K. Zalewski, *Phys. Rev. C* **82** (2010) 034911, *Phys. Rev. C* **85** (2012) 029903, [arXiv:1008.4690 \[hep-ph\]](#).
- [14] V. Vechernin, *PoS QFTHEP2013* (2013) 055, [arXiv:1305.0857 \[hep-ph\]](#).
- [15] UA5 Collaboration, R. E. Ansorge et al., *Z. Phys. C* **37** (1988) 191.
- [16] S. Uhlig, I. Derado, R. Meinke, and H. Preissner, *Nucl. Phys. B* **132** (1978) 15.
- [17] ATLAS Collaboration, *JHEP* **1207** (2012) 019, [arXiv:1203.3100 \[hep-ex\]](#).
- [18] ALICE Collaboration, J. Adam et al., *JHEP* **1505** (2015) 097, [arXiv:1502.00230 \[nucl-ex\]](#).
- [19] PHOBOS Collaboration, B. B. Back et al., *Phys. Rev. C* **74** (2006) 011901, [arXiv:nucl-ex/0603026 \[nucl-ex\]](#).
- [20] STAR Collaboration, B. I. Abelev et al., *Phys. Rev. Lett.* **103** (2009) 172301, [arXiv:0905.0237 \[nucl-ex\]](#).

- [21] R. S. Bhalerao, J.-Y. Ollitrault, S. Pal, and D. Teaney, *Phys. Rev. Lett.* **114** (2015) 152301, [arXiv:1410.7739 \[nucl-th\]](#).
- [22] J. Jia, S. Radhakrishnan, and M. Zhou, [arXiv:1506.03496 \[nucl-th\]](#).
- [23] M. Gyulassy and X.-N. Wang, *Comput. Phys. Commun.* **83** (1994) 307, [arXiv:nucl-th/9502021 \[nucl-th\]](#).
- [24] Z.-W. Lin, C. M. Ko, B.-A. Li, B. Zhang, and S. Pal, *Phys. Rev. C* **72** (2005) 064901, [arXiv:nucl-th/0411110 \[nucl-th\]](#).
- [25] ATLAS Collaboration, *JINST* **3** (2008) S08003.
- [26] ATLAS Collaboration, *Phys. Lett. B* **707** (2012) 330, [arXiv:1108.6018 \[hep-ex\]](#).
- [27] ATLAS Collaboration, *Phys. Lett. B* **710** (2012) 363, [arXiv:1108.6027 \[hep-ex\]](#).
- [28] ATLAS Collaboration, *Eur. Phys. J. C* **73** (2013) 2304, [arXiv:1112.6426 \[hep-ex\]](#).
- [29] M. L. Miller, K. Reygers, S. J. Sanders, and P. Steinberg, *Ann. Rev. Nucl. Part. Sci.* **57** (2007) 205, [arXiv:nucl-ex/0701025 \[nucl-ex\]](#).
- [30] GEANT4 Collaboration, S. Agostinelli et al., *Nucl. Instrum. Meth. A* **506** (2003) 250.
- [31] ATLAS Collaboration, *Eur. Phys. J. C* **70** (2010) 823, [arXiv:1005.4568 \[physics.ins-det\]](#).
- [32] ALICE Collaboration, K. Aamodt et al., *Phys. Lett. B* **708** (2012) 249, [arXiv:1109.2501 \[nucl-ex\]](#).

Appendix

Figure 11 shows the multiplicity distributions for three typical events in 10-15% centrality interval, normalized by the average distribution. Figure 12 shows the correlation of the FCal ΣE_T with the N_{ch}^{rec} distribution for the Pb+Pb events used in this analysis. Figure 13 is similar to Fig. 3 but show 2-D correlation functions in other centrality intervals. Figure 14 shows the removal of residual centrality dependence effects for 5-10% centrality interval, similar to Fig. 1. Figures 15 and 16 are plots complimentary to Figures 4 and 5, representing the correlation function projected in additional η_+ and η_- slices. Figures 17 and 18 present a subset of the information contained in Fig. 10.

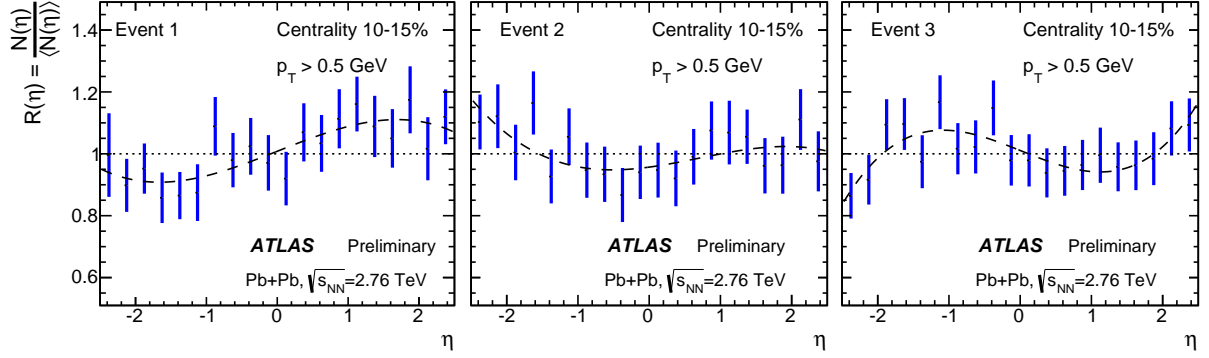


Figure 11: The multiplicity distributions of three typical events in 15–20% centrality interval. They are divided by the average distribution of all events in the same centrality interval. The dashed lines indicate fits to a third-order polynomial function.

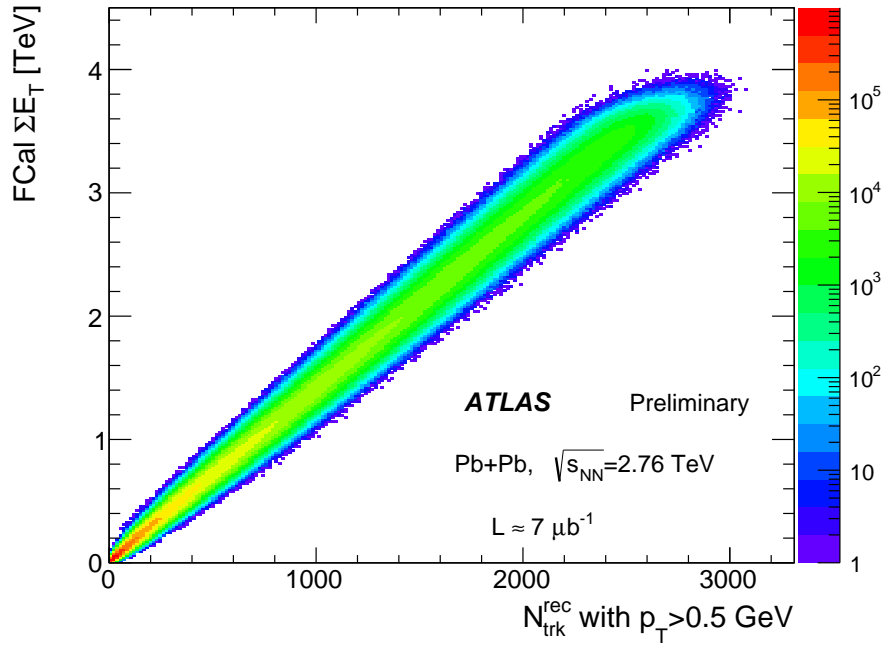


Figure 12: The correlation of total transverse energy deposited in the FCal ΣE_T and total number of reconstructed tracks $N_{\text{ch}}^{\text{rec}}$ for $p_T > 0.5$ GeV.

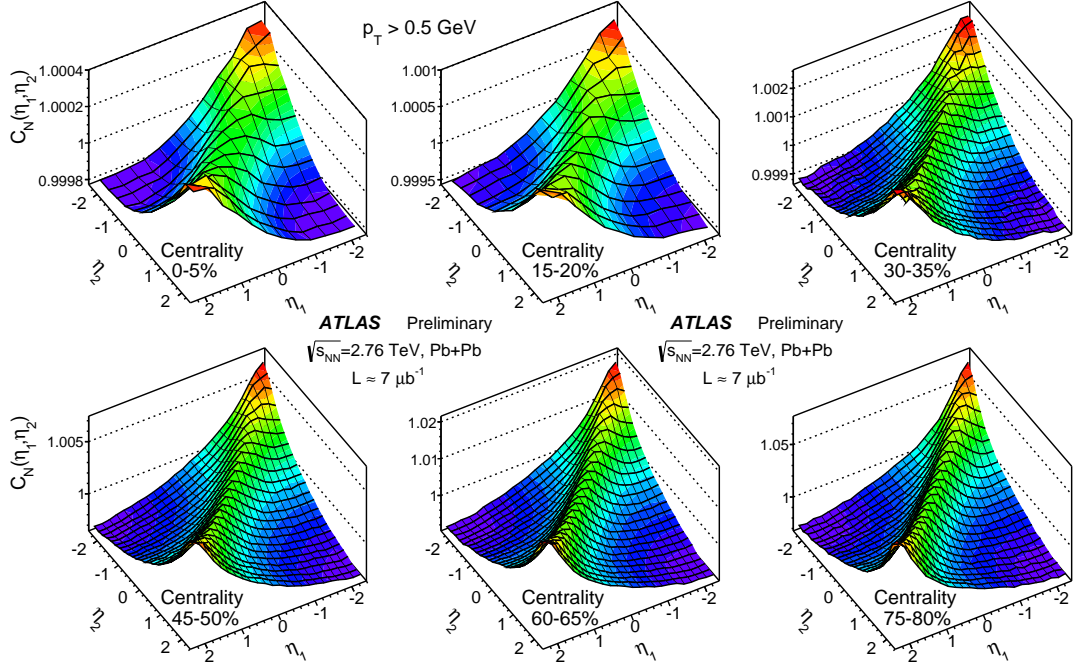


Figure 13: The 2-D pseudorapidity correlation function $C_N(\eta_1, \eta_2)$ in six centrality intervals.

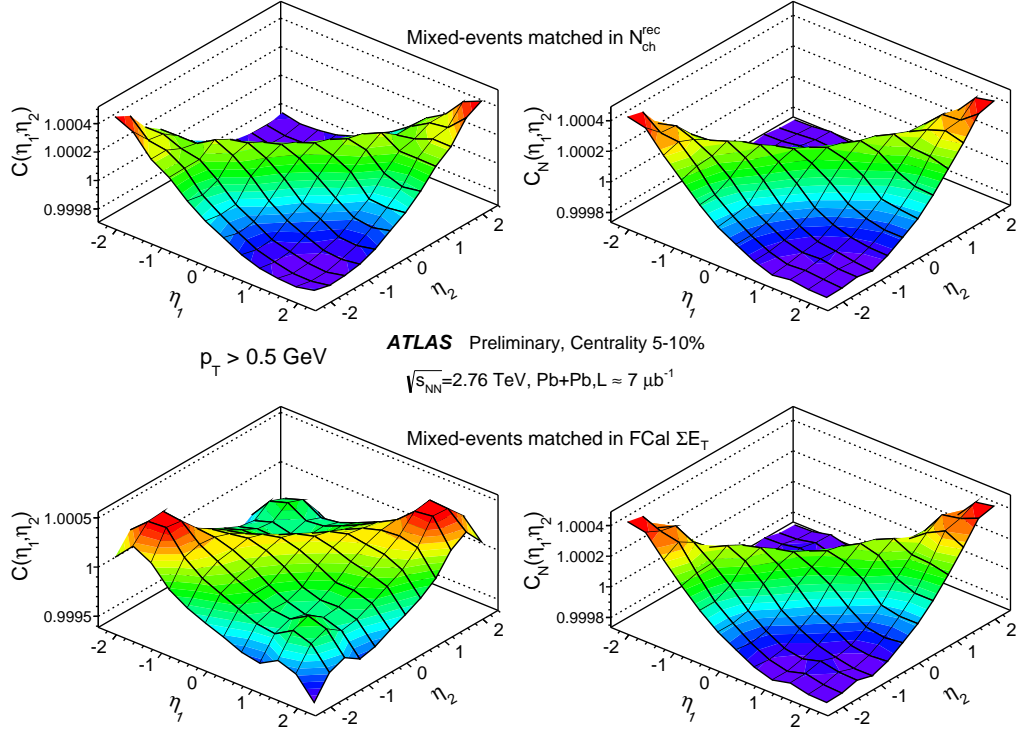


Figure 14: The correlation functions $C(\eta_1, \eta_2)$ (left panels) and $C_N(\eta_1, \eta_2)$ (right panels) in 5–10% centrality interval. The mixed-event pairs are obtained by matching two events in either narrow $N_{\text{ch}}^{\text{rec}}$ intervals (top panels) or narrow FCal ΣE_T intervals (bottom panels), where $N_{\text{ch}}^{\text{rec}}$ is the total reconstructed tracks for $p_T > 0.5$ GeV and ΣE_T is the total transverse energy deposited in the FCal over the pseudorapidity range $3.2 < |\eta| < 4.9$.

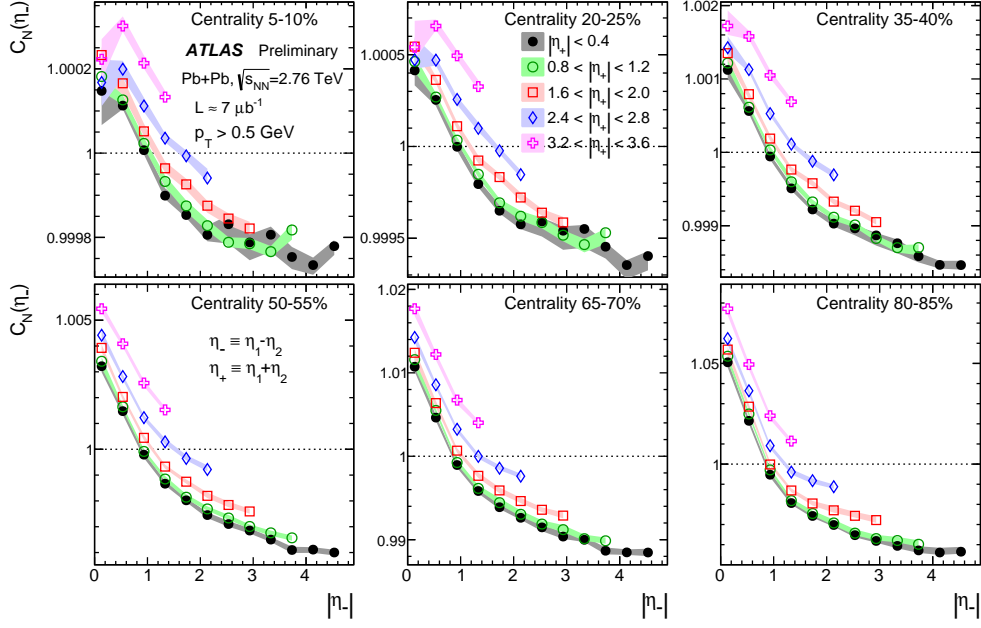


Figure 15: The 1-D correlation functions $C(\eta_-)$ with $\eta_- \equiv \eta_1 - \eta_2$ obtained by projecting the $C_N(\eta_1, \eta_2)$ in five narrow ranges of $\eta_+ \equiv \eta_1 + \eta_2$ indicated by the figure legend. Each panel represents results from one centrality interval. The shaded bands are the total uncertainties.

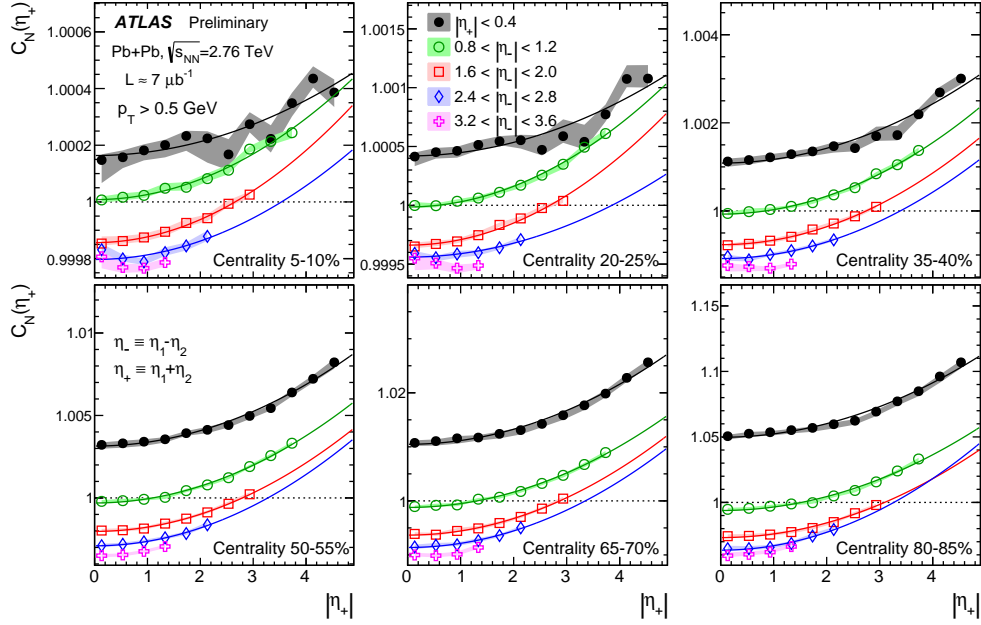


Figure 16: The 1-D correlation functions $C(\eta_+)$ with $\eta_+ \equiv \eta_1 + \eta_2$ obtained by projecting the $C_N(\eta_1, \eta_2)$ in five narrow ranges of $\eta_- \equiv \eta_1 - \eta_2$ indicated by the figure legend. The solid curves indicate the fits to Eq. 15. Each panel represents results from one centrality interval. The shaded bands are the total uncertainties.

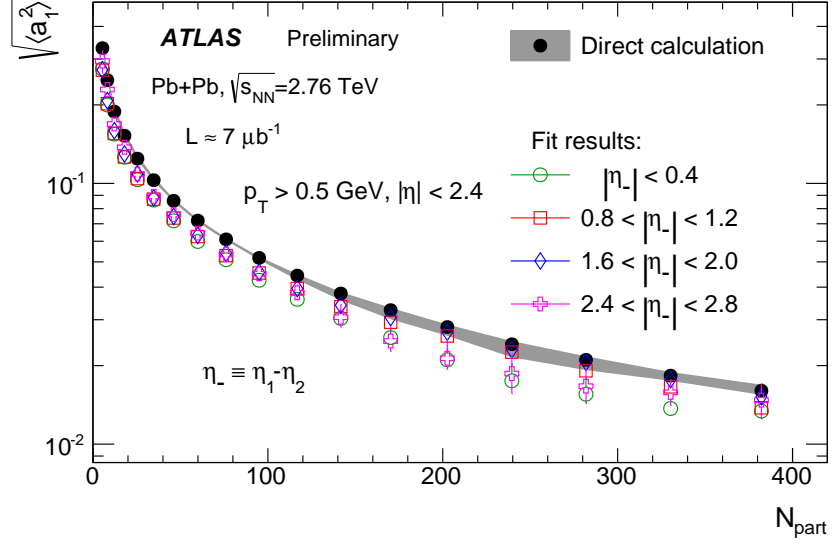


Figure 17: The centrality (in terms of total number of participating nucleons N_{part}) dependence of $\sqrt{\langle a_1^2 \rangle}$ calculated directly from the $C_N(\eta_1, \eta_2)$ (solid circles) and those obtained from fits shown in Fig. 5. The shaded bands or error bars are the total uncertainties.

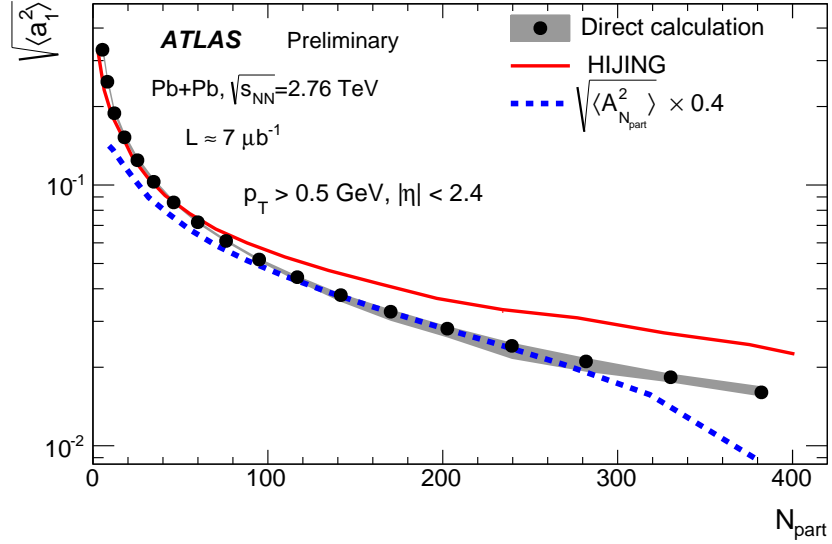


Figure 18: The centrality (in terms of total number of participating nucleons N_{part}) dependence of $\sqrt{\langle a_1^2 \rangle}$ calculated directly from the $C_N(\eta_1, \eta_2)$ (solid circles), HIJING model prediction (solid line) and the RMS values of $A_{N_{\text{part}}}$ from Eq. 16 (dashed line). The shaded bands are the total uncertainties.